View Article Online
DOI: 10.1039/D2FD00102K

ARTICLE

Plasmon-Driven Methanol Oxidation on PtAg Nanoalloys Prepared by Improved Pulsed Laser Deposition

–eceived 00th January 20xx,
Accepted 00th January 20xx

DOI: 10.1039/x0xx00000x

Junpeng Wang[a], Longfei Guo[a], Bowei Pan[a], Tao Jin[a], Zhen Li[a], Quan Tang[a], Pascal Andreazza[b], Yu Chen[c], Liang An[d], Fuyi Chen[a]*

Methanol oxidation reaction (MOR) is crucial in many energy-conversion devices. Although intensive efforts have been devoted to improving the MOR catalytic activity of Pt-based catalysts by treatment or alloying, enhancing MOR catalyst performance, utilizing solar energy has been less investigated. PtAg nanoalloys, combining the intrinsic catalytic activity of Pt toward MOR with the visible spectrum plasmonic response of Ag, are expected to be a good MOR catalyst for solar energy, however, it remains challenging to incorporate these immiscible elements into a nanoalloy in a controlled way using conventional synthetic techniques. Herein, we proposed a general strategy for alloying silver and platinum elements into single-phase solid-solution nanoparticles with arbitrarily desired composition by bonding pure Pt targets with pure Ag strips in an improved pulsed laser deposition. The as-prepared PtAg nanoalloys show two crystalline phases alloy and an average particle size of about 4 nm. To prove utility, we use the PtAg nanoalloy as support-free MOR catalysts anchored on the surface of glassy carbon electrode solidly and uniformly. The PtAg nanoalloys exhibit a mass catalytic activity of 3.6 A/mg, which is 4.5 times higher than that of commercial Pt/C catalyst. Besides, the PtAg nanoalloys exhibit a promising regenerability after reactivation by cyclic voltammetry. Furthermore, the MOR catalytic activity of PtAg nanoalloys increased by 16% under the irradiation of simulated sunlight, which is attributed to the surface plasmon resonance as ascertained from the UV-vis absorption spectra and photocurrent responses experiments. These studies are believed to provide a new strategy for the enhancement of MOR catalytic activity with visible light as driving force.

Introduction

Binary and multicomponent metallic nanoparticles, which are called nanoalloys, are of interest in wide spectrum of potential application, including catalysis,[1-8] electronics ,[9] energy storage [10, 11] and plasmonic imaging.[12-14] Nanoparticles alloyed with different elements could exhibit attractive material properties exceeding pure metal nanoparticles. [15, 16] For example, since Pd locates between Ag and Rh in the period table of elements, the solid-solution alloy of $Ag_{50}Rh_{50}$ could exhibit similar electronic properties to the counterparts of Pd. [17, 18] Moreover, the physical and chemical properties of nanoparticles can be significantly improved by the synergistic effect of the constituent elements. [19-21]

The current approaches toward the preparation of nanoalloys include the hydrothermal method, electrochemical deposition and physical vapour deposition. The colloidal method is a popular method.[5] Liu et al.[22] fabricated a new type of PtCu alloy nanoclusters and revealed that PtCu nanoclusters can substantially enhance the electrocatalytic activity toward the oxygen reduction reaction. Electrochemical deposition method is a low-cost method to prepare the nanoalloys. Wang et al. [23, 24] prepared the bimetallic AuNi nanodendrite and reported their high activity toward oxygen reduction reaction and borohydride oxidation reaction. Magnetron sputtering is one type of physical vapor deposition technique to produce thin film or nanoparticles. Yoo et al. [25] researched the Pt-La alloy prepared by magnetron sputtering and reported the relationship between d-band centers and catalytic activity in Pt_3M nanoalloy.

Recently, complete solid solution nanoalloys with classically immiscible constituent elements have been prepared.[26-28] High-temperature melt quenching is a scalable method to fabricate certain nonequilibrium solid solution nanoparticles, but only suitable

[a] State Key Laboratory of Solidification Processing, Northwestern Polytechnical University, Xian, 710072, China. E-mail: fuyichen@nwpu.edu.cn
[b] Interfaces, Confinement, Matériaux et Nanostructures, ICMN, Université d'Orléans, CNRS, Orléans, France
[c] Department of Physics, University of Strathclyde, John Anderson Building, 107 Rottenrow, Glasgow G4 0NG, UK
[d] Department of Mechanical Engineering, The Hong Kong Polytechnic University, Hung Hom, Kowloon, Hong Kong SAR, China

DOI: 10.1039/D2FD00102K

for some specific elements which are miscible at high temperature.[28, 29] Room-temperature synthesis of bulk immiscible Au-Rh, Au-Pt, Pt-Rh and Pd-Rh nanoparticles is realized by simple borohydride co-reduction of appropriate aqueous metal salt[30] where alloy composition can be tuned across the bulk miscibility gaps. Microwave synthesis of immiscible metals has been demonstrated to create some nanoparticles with unusual properties. For example, Au-Rh alloy nanoparticles have been found to have great potential in heterogeneous catalysis and Au-Pt alloy nanoparticles exhibit a high electrocatalytic activity for methanol oxidation reaction. However, these wet chemical methods usually require surfactant and harsh conditions, such as, harmful chemical substances and complicated experimental procedures. To prevent aggregation and to maximize the utilization of noble metals (Pt) in electrode catalysts for fuel cells, polymers, surfactants and ligands were used to improve dispersion, but they also decreased active areas of Pt due to organic molecules attached to the catalysts.

In this respect, pulsed laser deposition (PLD) [31] has emerged as a convenient, reliable approach to obtain kinetically stable alloys at room temperature in the miscibility gap of the alloy phase diagram.[32, 33] PLD process synchronizes with rapid cooling, which is similar to the quenching of liquid metal, and can effectively limit the rate of atom diffusion and segregation.[34]

The techniques to prepare bimetallic nanoparticles by pulsed laser ablation involve the ablation of alloy target, which is the easiest approach to control the final chemical constitution of the as-prepared nanoparticles.[27] However, this method is limited to miscible parent metals. For parent metals that are immiscible, e.g., Ag-Rh, the bulk parent metals need to grounded down into powder and pressed into targets. This method is apparently costly not only for the preparation of metal targets but also for the difficulty in recycling metal from the alloyed targets. Therefore, it is still a challenging task to fabricate alloy nanoparticles solid solution which is miscible at an atomic level from the binary transition metal systems with a large miscibility gap.

Herein, we develop a new approach to synthesize various PtAg alloy nanoparticles with different composition by bonding pure Pt targets with pure Ag strips in an improved pulsed laser deposition. Though Pt and Ag have a large miscibility gap in the bulk,[35, 36] the solid solution phase of PtAg nanoparticles with size of about 4 nm is obtained by this method. To the best of our knowledge, this is the first work demonstrating the direct preparation of alloyed PtAg nanoparticles using this technique. The PtAg nanoalloys showed high electro-catalytic activity toward methanol oxidation reaction (MOR). Its MOR mass catalytic activity reached 3.6 A/mg, which is 4.5 times higher than that of the commercial Pt/C catalysts, and achieved 1.16 times enhancement under the irradiation of simulated sunlight than that of without irradiation. The PtAg nanoalloys still well anchor on the glass carbon electrode without peeling off after long time for electrochemistry and stability test. It is noteworthy that this fabrication strategy can be used to prepare other binary and multicomponent metallic nanoparticles.

Experimental Section

Materials:

Platinum and silver target were purchased from Yipin Chuancheng (Beijing) technology Co., Ltd. Ethanol (C_2H_5OH, > 99.7%) and perchloric acid ($HClO_4$ > 70.0%) were purchased from Tianjin Fuyu Fine Chemical Co., Ltd. Potassium hydroxide (KOH ≥ 85.0%) and methanol (CH_3OH > 99.5%) was obtained from Guangdong Guanghua Sci-Tech Co., Ltd. Pt/C catalyst (20 wt %) was available from Johnson Matthey Fuel Cells. Oxygen (O_2) and nitrogen (N_2) gases were obtained from Xi'an Teda cryogenic equipment Co., Ltd. All chemicals used in this experiment were of analytical grade or of high purity grades. Ultrapure water (18.25 MΩ cm) was used throughout the experiments.

Synthesis of PtAg catalysts.

Glass carbon electrode (GCE 0.196 cm^2) was polished with 300 and 50 nm alumina slurry, followed by cleaning with ultrapure water and ethanol before being used. Nano polycrystal PtAg alloy were deposited on glass carbon electrode by the Pulsed Laser Deposition under the vacuum of $2x10^{-6}$ mbar. The energy of the nanosecond Q-switched Nd:YAG laser (EKSPLA, Lithuania) was 200 mJ/pulse with a wavelength of 266 nm, beam diameter of 1 mm and it was operated at the frequency of 1-10 Hz. The delay between flashlight and Q-switched was set to 2150 unit (unit = 0.25 μ s). A schematic illustration of PLD is shown in figure.1. Pt-Ag target was prepared from a pure platinum target (99.99% pure, 0.2 mm thick) on which silver strips (99.99% pure, 0.2 mm thick) were distributed radially and uniformly as shown in figure.1b. Pt-Ag targets were fabricated by varying number of the Ag strips. The Pt-Ag target was kept rotating continuously for the purpose of ablation on the surface of the target. Each laser pulse ablated very small amount of target to create a plasma plume, then the ablation plume was ejected from the target toward the substrate (GCE). The frequency of laser was firstly set at 1 Hz to remove the oxide layer of target. During the deposition, the frequency of laser was set at 10 Hz to deposit the PtAg nanoalloy on the GCE with 27000 laser pulses. In order to obtain the homogeneous deposition, the glass carbon electrode was fixed on the rotary sample platform. The distance between the glass carbon electrode and the target was around 5 cm. The entire process above was carried out in a stainless steel chamber with ultra-high vacuum. Besides, a pure silver target and platinum target were used to prepare pure silver and platinum catalyst. For the pure Pt NP catalyst, the final thickness of the fabricated samples was measured by the quartz crystal oscillation. For the PtAg NP catalyst, the mass of Pt was based on the ratio of Pt in the ablation track.

Physical Characterization

The phase structure of the samples was characterized by X-ray diffraction (Maxima XRD-7000) using Cu Kα irradiation with a grazing incidence of 1°. The intensity profiles with respect to the q scattering vector modulus were analysed thank to spectrum simulations on the basis of the Debye equation from nanoparticle models of PtAg A1 alloyed crystalline phases[37, 38]. These models were obtained by geometrical construction with various size and various composition. q is the magnitude of the wave vector difference ($q = 4\pi\sin\theta/\lambda$), 2θ is the angle between the incoming and outgoing x-rays, and λ is the wavelength of the x-rays used. The morphology and microstructure of the as prepared samples were investigated using the scanning electron microscope (FEI Verios G4) and Atomic Force Microscope (Bruker Dimension Icon) in tapping mode. High resolution transmission electron microscope (HRTEM) images were obtained by transmission electron microscopy (FEI Talos F200X and FEI Themis Z) and the EDX spectroscopy was used to record the elemental compositions. X-ray photoelectron spectroscopy (XPS) of the PtAg alloy films was recorded on a Thermo Scientific ESCALAB 250 Xi instrument under ultrahigh vacuum of 9^{-10} mbar. Using a monochromatic Al Kα radiation (hv =1486.6 eV) to examine the surface component and electronic structure. The spectra were calibrated by the carbon peak (C 1s) at 284.6 eV. The photoelectronic properties of catalysts was characterized by simulated solar light radiation (AM 1.5G, 100 $mWcm^{-2}$) and monochromatic LED light system (wavelength of 385 nm and 640 nm, respectively).

Electrochemical characterization

The electrochemical measurements were performed on a classic three-electrode system. The working electrode was the Pt-Ag alloy directly deposited on the GCE. A Hg/HgO electrode (1 M KOH) and a Pt film electrode (1 cm^2) were used as reference electrode and counter electrode, respectively. As the Pt and Ag had the different sputtering yields under the same deposition condition, in the beginning, the correction factor between the Pt/Ag atomic ratio in the deposited film and the area covered by Pt/Ag in the laser ablation race-track were obtained. All the samples were deposited by 27000 pulse in the same time for 45 mins. Loading amounts of metal Pt for the $Pt_{25}Ag_{75}$, $Pt_{50}Ag_{50}$, $Pt_{75}Ag_{25}$ and Pt catalysts were calculated at 8.2 μg/cm^2, 9.7 μg/cm^2, 11.9 μg/cm^2 and 14.1 μg/cm^2, respectively. A mixed aqueous solution of 1.0 M KOH and CH_3OH 1.0 M was used as the electrolyte solution to characterize the electrocatalytic activity of the PtAg NPs catalysts toward MOR. Before electrochemical measurement, the electrolyte solution was deoxygenated by bubbling with high purity nitrogen at least 30 minutes.

The catalysts as prepared were electrochemically cycled from -0.9 to 0.3V (Hg/HgO) at 50 mV/s for 15 cycles to clean the surface. After the catalysts were cleaned, an extended cyclic voltammetry (CV) from -0.9 to 0.8V at 50 mV/s for 10 cycles was conducted to activate the surface of the catalysts. The electrochemical MOR was conducted by CV at the potential scan rate of 50mV/s. A simulated solar light source (AM 1.5G, 100 $mWcm^{-2}$) was used to characterize the plasmon enhanced electrocatalytic activity of PtAg NPs catalysts in the MOR. The electrochemical surface area (ECSA) of the as-prepared catalysts was determined by measuring hydrogen adsorption charge at room temperature in nitrogen saturated 0.1 M $HClO_4$ electrolyte solution. For the comparison, the commercial catalysts Pt/C calculated as 0.1 mg/cm^2 (Johnson-Matthey, 20 wt%) was used as the baseline catalyst. To ensure the reproducibility of measurements results, all the experiments were carried out at least three times repeatedly. All electrochemical tests were carried out on a CHI660C electrochemical workstation.

Results and Discussion

Characterization of PtAg nano-polycrystalline catalysts

PtAg nano-polycrystalline (NP) samples were prepared using a Pulsed Laser Deposition system. This method allows to produce films of proportions without requiring the PtAg alloy target of specific components. In an innovative synthesis as shown in figure 1, the growth conditions of PtAg NP during depositing were optimized by varying the rate of Pt in PtAg NP with a suitable distance of 5cm between the target and substrate and depositions of 27000 laser pulses. A series of PtAg NP samples were prepared, named as Pt, $Pt_{75}Ag_{25}$, $Pt_{50}Ag_{50}$, and $Pt_{25}Ag_{75}$. As the Pt and Ag had the different sputtering yields under the same deposition condition, in the beginning, the correction factor between the Pt/Ag atomic ratio in the deposited film and the area covered by Pt/Ag in the sputtering race-track were obtained. The deposition yields were estimated using the nanoscale film thickness gauged in the PLD chamber and AFM. The composition of the prepared Pt/Ag samples determined by EDS approximately equals to the designed value, within a margin of error. Due to differences of melting point between Pt and Ag, the ablated area per laser shot is smaller than the lateral size of the Ag strips. For pure Pt and pure Ag targets, the yield of Ag is larger than that of Pt under the same conditions. The PtAg NP catalyst was synthesized as shown in figure 1 b. The ablated Ag and Pt were ejected from the binding target in a highly forward-direction plasma plume. As the target and electrode substrate were rotating in 15 r/min. The plasma plume of Ag and Pt was alternately quenched on the substrate. Since the laser intensity was set by adjusting the delay between flashlight and Q-switched, the average yield is less than an atom-layer thickness in a cycle. The alloying phenomenon of Pt and Ag was observed in the experiment. However, it is under studied for the specific alloying mechanism where the Pt and Ag atoms was surface-reconstructed when the vapor phase was quenching on the substrate.

The morphology and structure of the as-obtained PtAg NP were firstly examined by field-emission scanning electron microscope (FE-SEM), atomic force microscopy (AFM) and transmission electron microscopy (TEM). The Pt and PtAg NP present porous structure, like the sponge that is in sharp contrast to the highly uniform Ag NP (figure 2, S1 and S2). AFM measurement shows that the height of Pt and PtAg NP are at the range of 3.2-3.8 nm, while the height of Ag NP reached up to 7.6 nm, which is two times of the former four samples. These finding confirmed that the Ag target had a higher sputtering rate than Pt and PtAg target in the same condition. It should be mentioned

View Article Online
DOI: 10.1039/D2FD00102K

that the grain refinement not only improves the mechanical performance, but also increase the surface roughness of the PtAg NP catalyst. From the image of the SEM (figure S1), it can be noted that Pt, PtAg and Ag NP were uniformly distributed on the glassy carbon electrode. The average size of the $Pt_{75}Ag_{25}$, $Pt_{50}Ag_{50}$ and $Pt_{25}Ag_{75}$ NP is less than that of Pt and Ag NP, indicating that alloying of Pt and Ag may restrict excessive growth of PtAg NP. This is due to the large lattice mismatch between Ag and Pt, which hinders epitaxial growth of either monometallic.[39] Therefore, this approach of alternating deposition is an effective way to obtain smaller size alloy nanoparticles.

From the figure 3a&b, it can be found that the Pt50Ag50 nano-particles were formed from self-assembled sub-10 nm PtAg nano-crystals. This large PtAg NP results from the coalescence of the sub-10 nm grains during the particles growth. The PtAg NP catalyst was further investigated using the high-angle annular dark-field scanning transmission electron microscopy (HAADF-STEM). Figure 3c, d show the HAADF- STEM image of Pt50Ag50 NP using an electron microscope with aberration correction systems. The Pt50Ag50 NP displayed clear lattice fringes, indicating a good crystallinity. The marked square in figure 3d and the corresponding fast Fourier transform (FFT) patterns (in figure 3d inset) demonstrate that Pt50Ag50 NP displayed clear spacing of 0.232 nm, 0.203 nm and 0.142 nm correspond to the (111), (200) and (220) planes of PtAg alloy, respectively. Figure 3e display the elemental mappings of individual elements. It can be found that the PtAg NP is composed of elements Pt and Ag. According to the location and intensity, both Pt and Ag are homogeneously

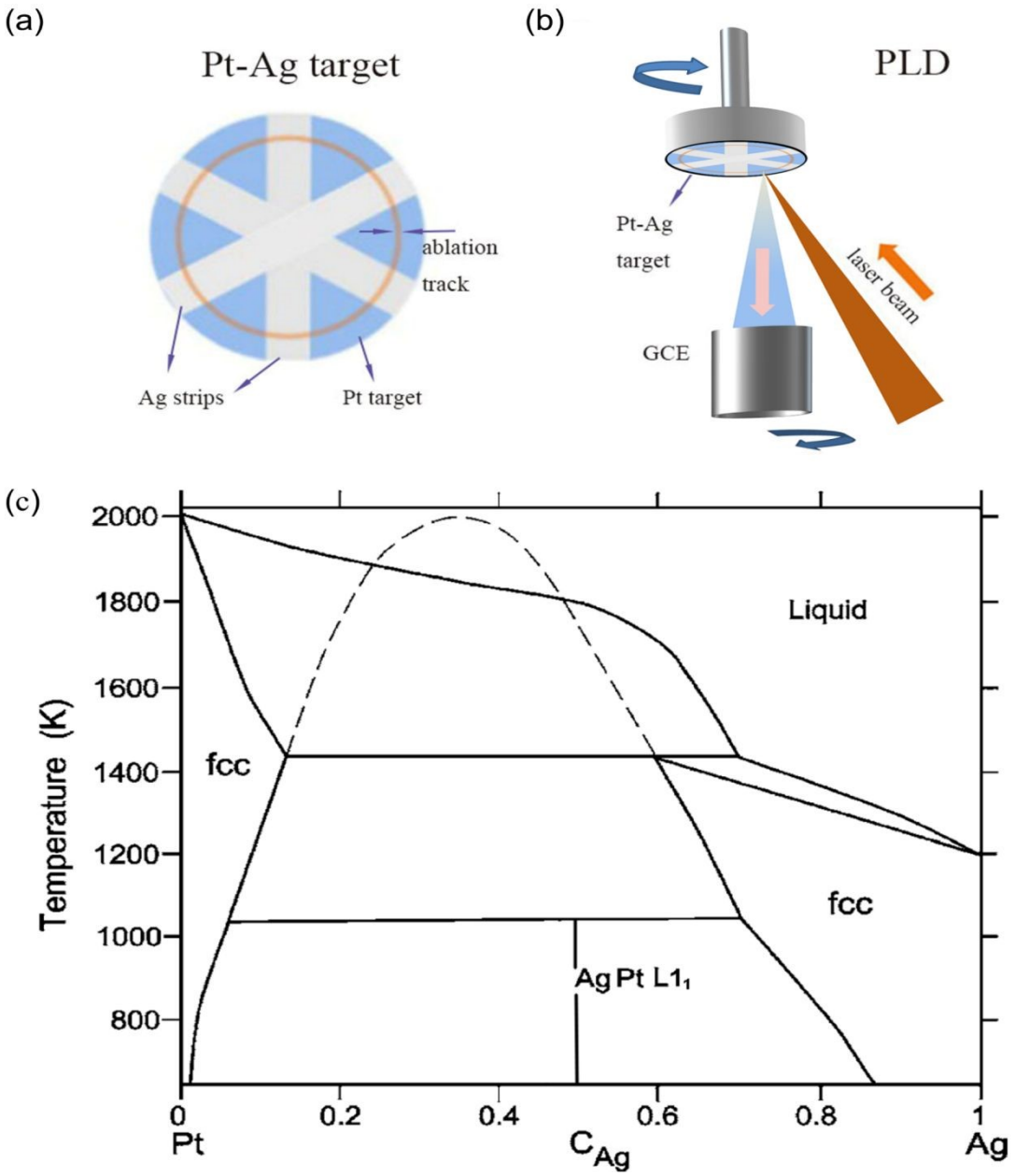

Figure 1. The improved pulsed laser deposition (PLD) method. (a) Pt-Ag Target, the Ag strips distribution on the Pt target, the dotted rings represent the erosion race - track). (b) Schematic illustration of the pulsed laser deposition (PLD) method. (c) Pt-Ag phase diagram based on the assessed experimental phase diagram from Durussel1996 and confirmed by sluiter2006.[40, 41]

distributed throughout the PtAg nanoalloy. Furthermore, the EDS line scanning analysis as shown in figure 3f, reveals that the atomic ratio of Pt:Ag is approximately 50:50, indicating that the two metals distribute homogeneously.

View Article Online
DOI: 10.1039/D2FD00102K

From the figure S3 and S4, it can be noted that the diameter distribution of the PtAg NP ranged from 2 nm to 10 nm. In the figures S3 b and d, the HAADF-STEM images show that the PtAg alloy possesses well-dispersed ultrafine PtAg NP. The average sizes of the Pt50Ag50 NP and Pt25Ag75 NP were 4.0±0.5 nm and 5.0±0.5 nm, respectively, which are in accordance with the feature high-resolution bright field images (figure 3a, b and figure 5e, f). Furthermore, the majority diameters of the PtAg NP are only 4-5 nm with a large amount lattice fringes, indicating that it has a good crystallinity. The marked square in figure 4b and the corresponding fast Fourier transform (FFT) patterns (in figure 4c) demonstrate that the Pt50Ag50 NP has well-defined lattice planes. The lattice of plane defects including grain boundary, twin grain boundary and faults.

TEM and geometric phase analysis (GPA) stress were further investigated to demonstrate the crystal defect of Pt50Ag50 NP. Figure 4(a, b) displays the HR-TEM image of the Pt50Ag50 NP, which reveals that the lattice fringe is 0.231 nm and 0.233 nm

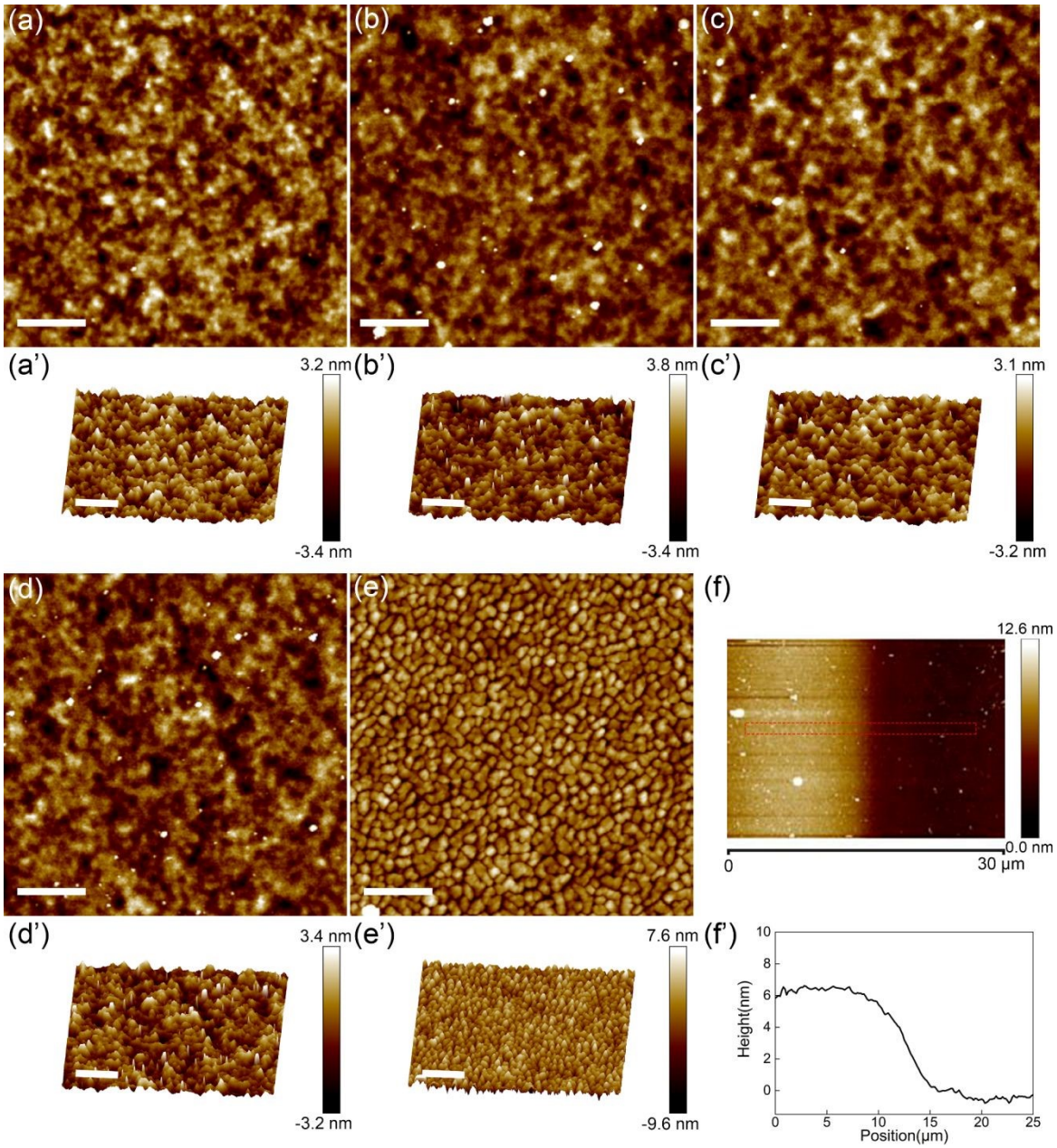

Figure 2. Morphology characterization of as-prepared samples. Tapping-mode AFM images of Pt NP (a), $Pt_{75}Ag_{25}$ NP (b), $Pt_{50}Ag_{50}$ NP (c), $Pt_{25}Ag_{75}$ NP (d), and Ag NP (e). Stereoscopic display of AFM images were corresponding to images of (a'), (b'), (c'), (d') and (e'), respectively. (f) Step of Pt NP sample deposition on the quartz plate. (f') The thickness of pure Pt NP synthesized by PLD for 45 min with 27000 pulses.

indexed to (111) face-center-cubic structure. The well-resolved lattice as shown in figure 4(b, e) indexed as crystal planes of (111) and (200) with the PtAg solid solution phase. This would also indicate that Ag and Pt had successfully inserted into the lattice of each other during the process of preparation by the PLD. Figure 4e reveals the twin planes of the PtAg nanostructure corresponding to red square of figure 4b, as the different atomic radii of Pt and Ag, the epitaxy direction can be changed during the process of crystal growth. GPA was conducted to display the defects and the uneven stress distribution verifies the existence of lattice strain in the Pt50Ag50 NP in figure 4(f-i). Furthermore, dislocation can contribute to the strain effect in the lattice plane. The presence of defects and interconnecting morphologies demonstrated that there was a weak degree of epitaxial growth between Pt and Ag.42 Compared to Pt50Ag50 NP, HRTEM and GPA stress of Pt50Ag50 NP were shown in figure 5, which exhibit few strain defects and dislocations at the same area. PtAg is thought to show an off-center core-shell structure because the subsurface is in a compressed state and a smaller subsurface impurity allows a better relaxation.43 Though, PtAg has the similar systems with a

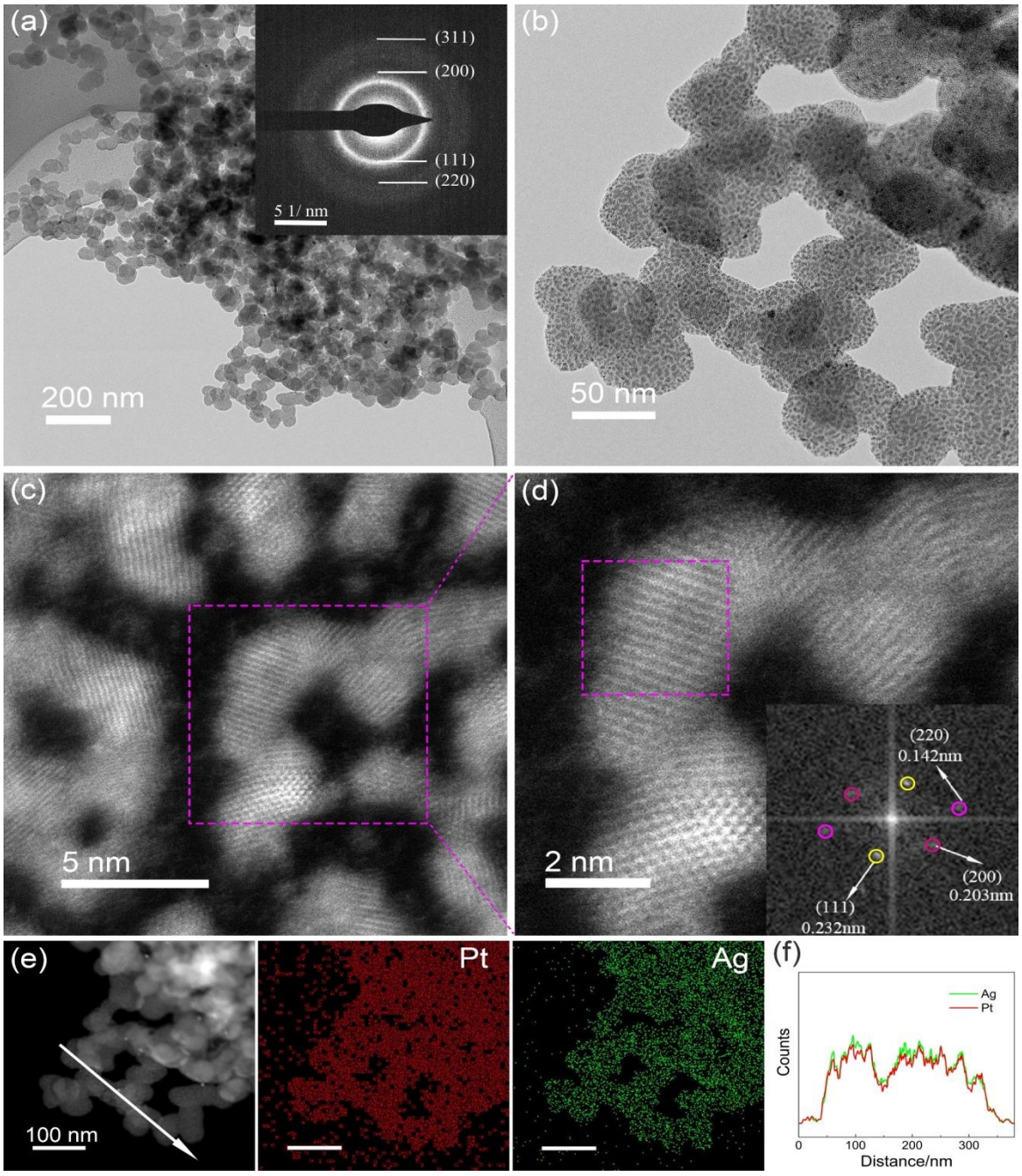

Figure 3. (a, b) Bright-field TEM images of $Pt_{50}Ag_{50}$ nanoparticles, with a selected-area electron diffraction patterns in b inset. (c, d) High-resolution HAADF-STEM images of $Pt_{50}Ag_{50}$ nanoparticles and Fourier transform of lattice images in marked square of (d). Revealing the diffraction spots corresponding to lattice spacing of the (111), (200) and (220) facets. (e) HAADF-STEM images and EDX elemental mappings of $Pt_{50}Ag_{50}$ NP. (f) EDX line profiles extracted from the typical lines in the HAADF-STEM image (e).

strong tendency to segregation, we find that as-prepared PtAg nanoalloys are mixed alloy, and the dislocation sustain the strain.

The formation of bimetallic PtAg NP in the co-deposition of Pt and Ag metals on the GCE were further investigated through XRD measurements. XRD analysis is able to reveal the average level of crystallinity, the nature of phases and their atomic fraction. The XRD patterns of PtAg NP with different average Ag atomic percentage were shown in figure 6a, and the XRD peak position for pure Pt and Ag were also presented as comparison. The main peak sequence is totally in agreement with the crystalline fcc A1 phase with (111), (200), (220), (311) and (222) planes. Qualitatively, all main peaks of $Pt_{75}Ag_{25}$, $Pt_{50}Ag_{50}$ and $Pt_{25}Ag_{75}$ samples, were lying with in both limits of the monometallic Pt and Ag (JCPDS reference) which is the signature of an alloyed state of the nanoparticles. However, spectra simulations and adjustments with experimental data reveal the presence of two crystalline phases: i) a majority alloy phase A with a lattice parameter which increases with the average composition in Ag; ii) a second alloy phase B with a stable lattice parameter a = 0.393 nm close to the pure Pt phase, this phase is minority with an atomic proportion that decreases as the average composition in Ag increases (from 5%, 10%, 35% for Pt75Ag25, Pt50Ag50 and Pt25Ag75 respectively). If we don't consider any stress effect (stress induced by surface could be neglected at this particle size), a composition can be deduced from a simple linear Vegard law. The phase B seems to be Pt-rich, stable for all sample with less than 10% in Ag atoms. The deduced composition of the phase B which varies, is richer in Ag than the average composition, as :

- For Pt25Ag75 sample: 85-90% Ag composition with a = 0.401+-0.001 nm
- For Pt50Ag50 sample: 70-75% Ag composition with a = 0.4045+-0.001 nm
- For Pt75Ag25 sample: 40-45% Ag composition with a = 0.406+-0.001 nm

Figure 6 a1, b1, c1 show a zoom that evidence that the phase B/phase A ratio increase as the Ag to Pt atom average percentage decreases. The insertion of Pt into Ag lattice structures is limited in bulk at equilibrium (Figure 1c) to less than 20% in Ag, while the Ag insertion into Pt lattice is of less than 5%. The miscibility gap in bulk in partially transposes at the nanoscale. However, a surface segregation of Ag atoms in the A alloyed phase cannot be ruled out. In addition, the intensity profiles

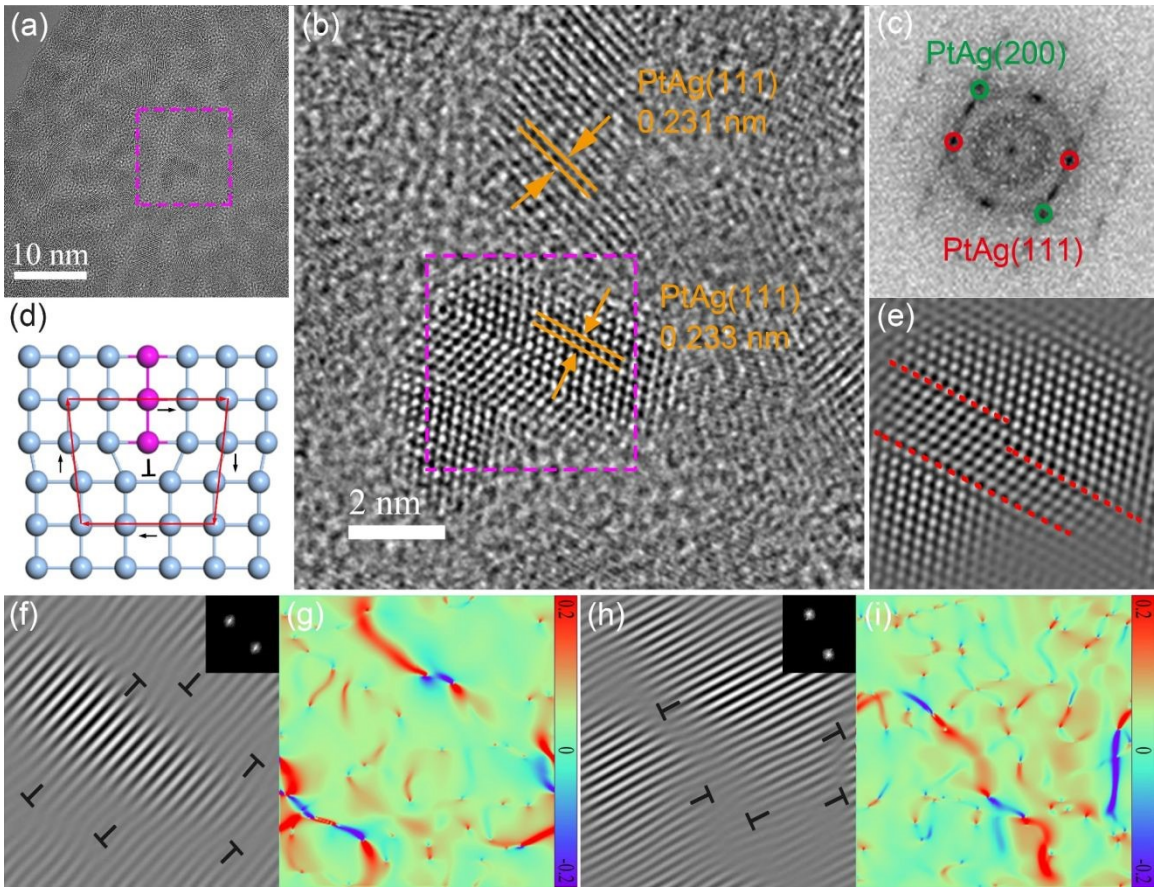

Figure 4. TEM and strain characterizations of $Pt_{50}Ag_{50}$ NP. (a) TEM image of $Pt_{50}Ag_{50}$ NP. (b) HRTEM image recorded from the marked square of (a). (c, e) The FFT and IFFT of the patterns of the marked region in the HRTEM image of the (b). (d) Schematic diagram of edge dislocation. (f, h) IFFT patterns of the (111) and (200) planes corresponding to the FFT patterns of the image (g). (g, i) Strain distributions of the (111) and (200) planes, respectively (The negative and positive values on the scale bar represent compressive and tensile strain).

View Article Online
DOI: 10.1039/D2FD00102K

(figure 6) are not in agreement with a perfect crystalline or homogeneously strained nanoparticles, as disordered structures 37, 44. Calculated nanoparticle structures (around 5 nm in size) with same behaviour in the (111)-(200) peak region 44, 45shows that the clusters contain (1 1 1) twins and stacking faults (planar defects), which induce small strain, mainly in planes disoriented with respect to the (1 1 1) plane, such as (0 0 2) (see in figure 6c-inset).

To investigate the origin of enhanced catalytic activity of the as-prepared PtAg NP, their electronic structures were examined using X-ray photoelectron spectroscopy (XPS). By comparing the survey spectra of PtAg NP and Pt, peaks belonging to Pt and Ag were clearly observed for PtAg NP, indicating the formation of bimetallic PtAg nanostructures. The binding energies of Pt4f5/2 and Pt4f7/2 of $Pt_{75}Ag_{25}$, $Pt_{50}Ag_{50}$ and $Pt_{25}Ag_{75}$ are blue-shifted apparently than those of pure Pt with increase of Ag content, which is in agreement with the XRD results (figure 6 and table 1A). Furthermore, the binding energies of Pt4f7/2 and Ag 3d5/2 have significant linear correlation with the mole fraction of Ag in the PtAg NP catalysts (figure-S5). The shifts of binding energies for Pt and Ag in the PtAg NP catalysts demonstrate an electronic structure change of Ag and Pt, which could be attributed to the electronic interaction between the atomic orbitals of Ag and Pt.46, 47 As Pt is more electronegative than Ag, electrons will shift from Ag to Pt sites. The Pt 5d bands was partially filled by the increased charged density of surface Pt atoms, which causes the d-band center downshift and weakens the chemisorption of CO_{ad}.[48]

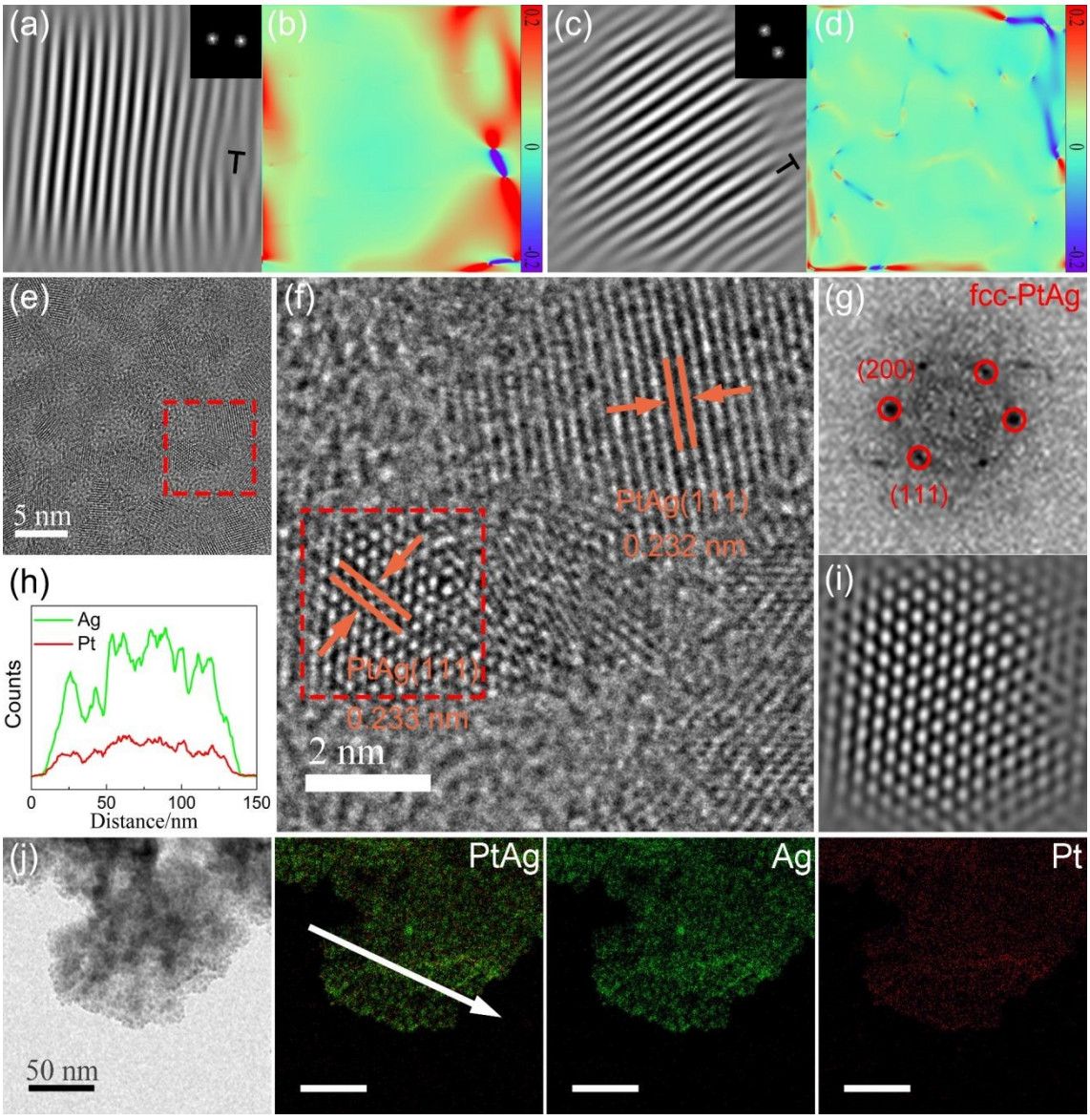

Figure 5. TEM and strain characterizations of $Pt_{25}Ag_{75}$ NP. (a, c) IFFT patterns of the (111) and (200) planes corresponding to the FFT patterns of (g). (b, d) Strain distributions of the (111) and (200) planes, respectively (The negative and positive values on the scale bar represent compressive and tensile strain). (e) TEM image of $Pt_{50}Ag_{50}$ NP. (f) HRTEM image recorded from the marked square of (e). (g, i) The FFT and IFFT of the patterns of the marked region in the HRTEM image of the (f). (h) EDX line profiles extracted from the typical lines in the HAADF-STEM image. (j) TEM, HAADF-STEM images and EDX elemental mappings of $Pt_{50}Ag_{50}$ NP.

In addition, the shifts in binding energies also demonstrate that Pt and Ag are well alloyed in the PtAg NP. To further decipher the impacts of alloying to PtAg NP catalysts, XPS was performed to determine the valence band spectra (VBS) of Pt and PtAg NP, as shown in figure 7d. The d-band center of the PtAg NP is far away from the Fermi energy level than that of pure Pt, further indicating that the alloying of PtAg modify the electronic structure after the PLD. The modification of d-band center for PtAg NP may tune the absorption energy of reactant, intermediate, and products and thus improve the activity of PtAg NP catalysts. [49]

Electrochemical performance of PtAg NP catalysts

The electrochemical performance of as prepared PtAg NP of five different compositions were evaluated at room temperature and compared with monometallic Pt and Ag NP, and commercial Pt/C (20 wt%). The electrochemical active surface area (ECSA) was calculated by the hydrogen desorption region of cyclic voltammogram curves (CVs) recording from 0.03 V-1.57 V vs. RHE in the nitrogen saturation aqueous solution containing 0.1 M $HClO_4$ at the scanning of 50 mVs. As shown in figure S6, the hydrogen adsorption/desorption process took place from 0.03 V to 0.40 V and region of surface metal oxidation/reduction occur during 0.5 V and 1.3 V for Pt and PtAg NP. The ECSA of the Pt NP, $Pt_{75}Ag_{25}$ NP, $Pt_{50}Ag_{50}$ NP and $Pt_{25}Ag_{75}$ NP were 8.57, 13.3, 35.6, 28.5 $m^2\ g^{-1}_{Pt}$, respectively. In contrast, for the pure Ag NP (figure S7), no characteristic peaks were observed for the hydrogen adsorption/desorption. In the negative scan, the main reduction peak located around 0.6 V vs RHE can be associated with the reduction of Pt(II) oxide (figure S6).[45] As shown in the figure S6, the reduction peak appeared at around 0.66V that can be ascribed to the reduction of Ag oxide and is more positive than that of Pt. The reduction peaks of Pt and Ag overlapped in the PtAg NP alloy of $Pt_{75}Ag_{25}$, $Pt_{50}Ag_{50}$ and $Pt_{25}Ag_{75}$ NP, suggesting that there was a synergistic effect between Ag and Pt atoms .[46] As shown in the figure S7, the oxidation peak of Ag located at about 0.79 V and the oxidation peaks of

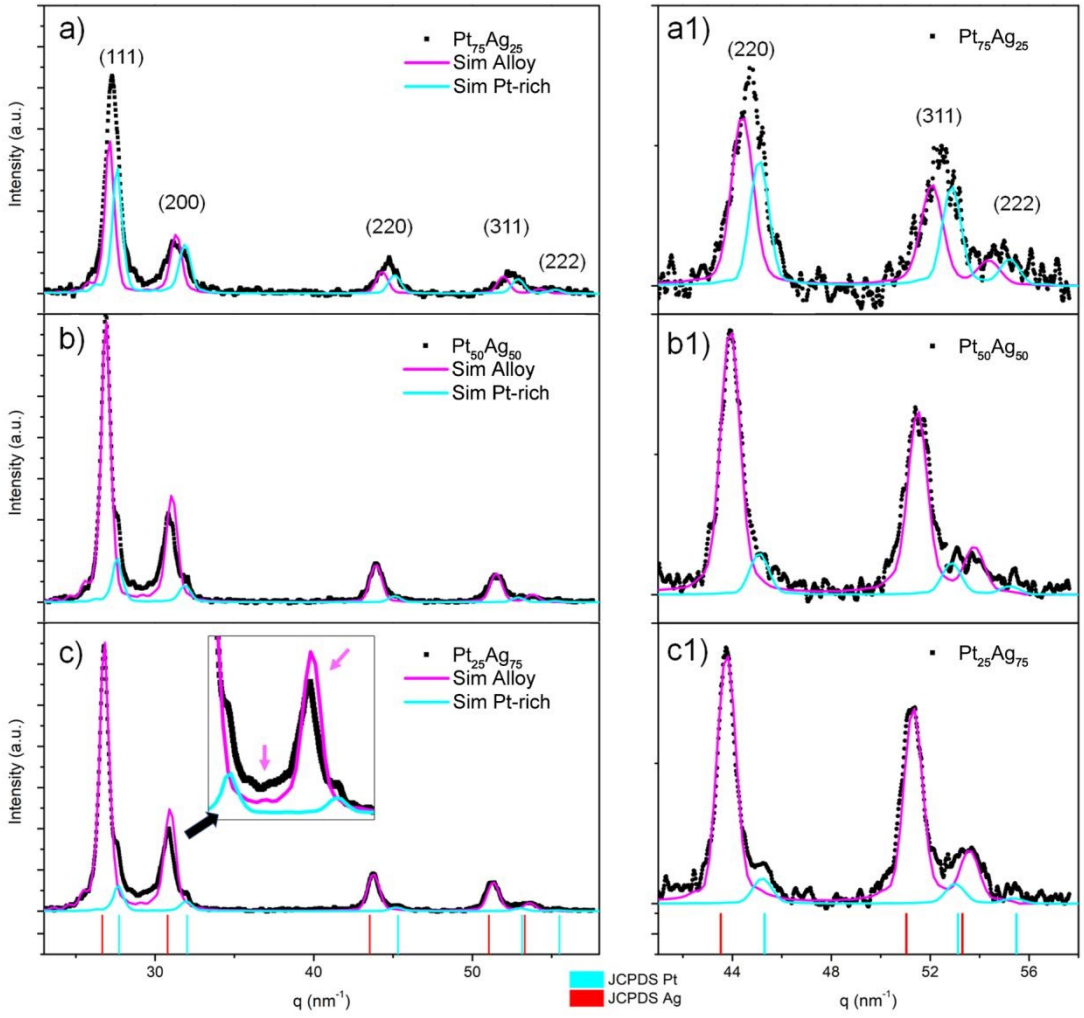

Figure 6. (a, b and c) XRD patterns of $Pt_{75}Ag_{25}$, $Pt_{50}Ag_{50}$ and $Pt_{25}Ag_{75}$ samples respectively: experimental spectra (black dots), simulated spectra of alloyed A phase (magenta line) and simulated spectra of alloyed B phase (cyan line). The standard Ag (JCPDS no. 04-0783) and Pt (JCPDS no. 04-0802) patterns are selected as the bar diagram at the bottom. In (c-inset): The arrows show the difference between perfectly crystalline nanoparticles simulated spectrum (line) and the experimental spectrum that is characteristic to the internal defects as twins and staking fault; (a1, b1 and c1) zoom of (220), (311) and (222) peak region corresponding to $Pt_{75}Ag_{25}$, $Pt_{50}Ag_{50}$ and $Pt_{25}Ag_{75}$ samples respectively.

View Article Online
DOI: 10.1039/D2FD00102K

the PtAg NP were at about 1.24 V (figure S6).The Ag oxidation peaks shift noticeably positively for the PtAg NP alloy catalyst, suggesting that the electrochemical stability of Ag had been greatly enhanced after alloying with Pt.

Recent studies reported that Pt-based NP has good electrocatalytic performance toward oxidation of methanol or ethanol in alkaline electrolyte.[50, 51] Enlightened by these attractive structures, the electrocatalytic properties of the as-prepared PtAg NP catalysts were tested. As shown in figure 8 and S8, the Pt NP s, $Pt_{75}Ag_{25}$ NP s, $Pt_{50}Ag_{50}$ NP and $Pt_{25}Ag_{75}$ NP were initially investigated by CVs in 1 M KOH and 1 M CH_3OH+1 M KOH aqueous solution at a potential scan rate 50 mV s^{-1}, respectively. When the Ag NP was scanned positive of 1.12 V vs RHE, three characteristic oxidation peaks were observed at about 1.16 V, 1.23 V and 1.35 V, which correspond to the formation of the monolayer of Ag_2O film, the AgOH and Ag_2O bulk phase, respectively.[52, 53] The oxide reduction peaks of Ag were observed at about 1.05 V vs RHE, corresponding to the oxide reduction peaks of pure Ag, as shown in figure-S8. For the $Pt_{50}Ag_{50}$ and $Pt_{25}Ag_{75}$, the oxide reduction peaks of Pt located at around 0.6 V and 0.65 V, respectively. With the increase of Pt content, the reduction peak of Pt shifts negatively, indicating more stable oxide formation. The CV of PtAg NP showed redox peaks of Pt and Ag, suggesting that both elements have electroactivity at the surface.

Figure 8c, d show the CVs results of the $Pt_{50}Ag_{50}$ and $Pt_{25}Ag_{75}$ NP for electro-catalytic methanol oxidation reaction in N_2-saturated 1.0 M KOH with 1.0 M methanol aqueous solution. In order to reach a steady state, the CVs for MOR were repeated 20 cycles, and the 21th cycle of CV was used for investigation. The CV curves show typical methanol electro-catalytic oxidation features in the alkaline medium. [54, 55] At the potential range of 0.4-0.9 V, every CV curve shows two methanol oxidation feature peaks, which are associated with the forward scan and backward scan methanol oxidation peaks. In the forward scan, the current densities of MOR increase gradually until the appearance of anodic peaks and then decline by surface oxide formation or diffusion control.[56] The lower anodic peak during backward scan can be ascribed to the oxidation of accumulated carbonaceous species which are not oxidized completely during the forward scan.[57] Such carbonaceous specious accumulated on the surface of catalyst can poison the catalysts to lower its activity. In contrast with figure 8a, b the reduction peaks of Ag became smaller in 1.0 M KOH with 1.0 M methanol aqueous, which were consistent with the results of pure Ag CVs (figure S9), indicating some resistance to Ag oxidation due to the presence of methanol.

Figure 9a shows CVs of methanol electro-oxidation reaction for the Pt, $Pt_{25}Ag_{75}$, $Pt_{50}Ag_{50}$ and $Pt_{25}Ag_{75}$ NP. Two irreversible anodic peaks can be observed clearly during cyclic voltammetry. In the forward scan, the peak current density of $Pt_{50}Ag_{50}$ is 34.5 mA/cm^2, higher than that of $Pt_{75}Ag_{25}$ NP (28.2 mA/cm^2) and $Pt_{25}Ag_{75}$ NP (22.8 mA/cm^2), and almost 3 times that of pure Pt NP (12.6 mA/cm^2), indicating a very good electro-catalytic activity in alkaline solution compared with the other three catalysts. The MOR onset potential for the Pt, $Pt_{75}Ag_{25}$, $Pt_{50}Ag_{50}$ and $Pt_{25}Ag_{75}$ NP are 0.59, 0.58, 0.53 and 0.53 V vs RHE, respectively. The onset potential is defined as the methanol oxidation potential at which one-tenth of the peak current density is reached. Hence, negative shift of the onset potential compared with pure and PtC shows a great improvement in the kinetics toward MOR under the same test condition.[54] Furthermore, the ratio of I_f/I_b (of which I_f and I_b represent the forward and backward peak current density in MOR respectively) could be considered as important index for the evaluation of anti-poisoning ability.[53] The $Pt_{50}Ag_{50}$ NP catalyst displays the highest I_f/I_b ratio (20.7), in comparison to the other four electro-catalysts (7.4, 9.5, 6.4 and7.4 for Pt, $Pt_{75}Ag_{25}$, $Pt_{25}Ag_{75}$ NP and commercial Pt/C, respectively, displayed in Table S1), suggesting its superior CO_{ads} poison tolerance. This improvement of electro catalytic activity of the PtAg NP is mainly ascribed to: (1) the mesoporous structure with more crystal defects, as observed in figure (2. 3) and figure-S1, can supply abundant electrochemistry active sites for MOR. (2) Lattice strain, either tensile or compressive, can modify the surface electronic structure by adjust the distance between surface atoms[58, 59]. (3) Alloying of Pt and Ag, which results in the inhabitation of adsorption of CO ad species and modulation of binding energy as revealed by XPS (figure.7). Figure 9b displays the CV results of $Pt_{50}Ag_{50}$ NP and commercial PtC for MOR in 1.0 M KOH with 1.0 M methanol solution at room temperature. The peak current value of $Pt_{50}Ag_{50}$ NP for MOR is two times larger than that of commercial Pt/C. In addition, it can be noted that the onset potential of MOR with $Pt_{50}Ag_{50}$ NP has a 60mV negative shift (from 0.59 to 0.53 V) in comparison with the commercial Pt/C catalyst. The $Pt_{50}Ag_{50}$ NP exhibit a much higher catalytic performance than that of commercial Pt/C catalyst.

*Table 1 A summary of the measurement results from the X-ray photoelectron spectroscopy (XPS)**

Sample	Binding energy(eV)				XPS analysis[at%]		Ag/Pt (at/at)
	Ag		Pt		Ag	Pt	
	3d3/2	3d5/2	4f5/2	4f7/2			
Ag	374.2	368.2					1:0
$Pt_{25}Ag_{75}$	374.1	368.1	73.7	70.5	79.87	20.13	3:1
$Pt_{50}Ag_{50}$	373.8	367.8	74.3	70.9	53.79	46.21	1:1
$Pt_{75}Ag_{25}$	373.6	367.6	74.5	71.2	24.78	75.22	1:3
Pt			74.7	71.4			0:1

*All the binding energies values were calibrated by the C1s peak at about 284.6 eV

As shown in figure 9c, the calculated mass activity at 0.76 V vs RHE are 0.81, 0.89, 1.7, 2.97 and 3.6 A/mg for commercial PtC, Pt, $Pt_{75}Ag_{25}$, $Pt_{25}Ag_{75}$, and $Pt_{50}Ag_{50}$ NP, respectively. In particular, the mass activity of $Pt_{50}Ag_{50}$ NP is 4.5 times higher than that of commercial Pt/C catalyst. Furthermore, the mass activity of $Pt_{75}Ag_{25}$ and $Pt_{25}Ag_{75}$ are 2.1-fold and 3.7-fold higher than that of commercial Pt/C. Hence, the PtAg NP exhibited higher mass activity in comparison with commercial Pt/C. The electrocatalytic activity and durability of the PtAg NP catalysts for MOR were further investigated by the current (i) time (t) chronoamperometric measurement technique at 0.675 V vs RHE (figure 9d). Potentiostatic chronoamperometry measurement was conducted in 1.0 M KOH and 1.0 M methanol aqueous solution at 0.675 V. During the initial minute, the current densities of five catalysts decay quickly due to the unavoidable formation of Pt oxides and carbonaceous species on the surface of catalysts in the early stage of methanol oxidation.[60] However, all the PtAg NP display slower decay and the current density of $Pt_{50}Ag_{50}$ NP is much higher than $Pt_{25}Ag_{75}$, $Pt_{75}Ag_{25}$ NP and commercial Pt/C. In particular, at the end of 3600 s duration measurement, the $Pt_{50}Ag_{50}$ NP still maintain much higher current density (0.58 A/mg), which is 6.8 times higher than that of commercial Pt/C (0.12 A/mg), as shown in figure 9d. It is noted that $Pt_{25}Ag_{75}$ also performance better electrocatalytic activity (0.12 A/mg) than that of commercial Pt/C, which is 1.4 times higher than that of commercial Pt/C.

These results clearly show that the $Pt_{50}Ag_{50}$ NP is a kind of high stable catalyst for MOR in alkaline medium. Figure 9e presents three such consecutive reactivation cycles. We can see that there is no distinct activity loss after reactivation by cyclic voltammetry. Since no MOR electrocatalyst can achieve an indefinitely stability at present, obtaining activity recovery via cyclic voltammetry may be a decent choice for DMFC. CV curves of $Pt_{50}Ag_{50}$ NP toward MOR with various methanol concentrations are shown in figure S11. When the concentration of methanol was less than 2.5 M, the oxidation current monotonously increased at 0.745 V. The results demonstrate that process of MOR is controlled by diffusion of methanol which plays a major role when the methanol concentration varies in the range of 0.2-2.5 M. Figure S12 shows CV curves of MOR for $Pt_{50}Ag_{50}$ NP prepared by PLD with different substrate-target distance. The methanol oxidation peak current corresponding to 4 cm, 5 cm and 6 cm are about 28.8, 34.5 and 20.9 mA/cm^2, respectively, indicating that optimal substrate-target distance is 5 cm. The optimal substrate-target distance may be attributed the maximum yield on the substrate or the specific morphology. The mechanism that causes the higher

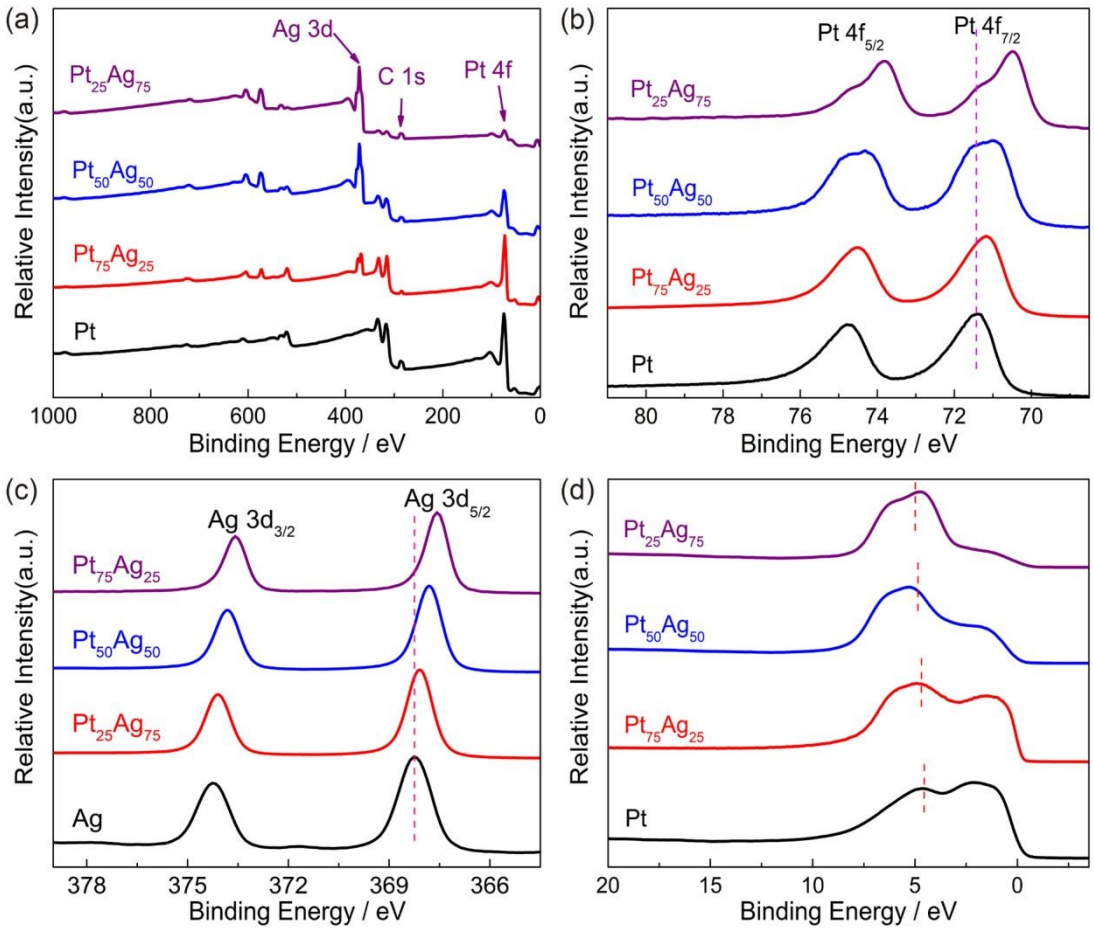

Figure 7. (a) The XPS survey spectra of the as-prepared $Pt_{75}Ag_{25}$, $Pt_{50}Ag_{50}$ and $Pt_{25}Ag_{75}$ nanoparticles, (b) High-resolution spectrum of Pt 4f region, (c) High-resolution spectrum of Ag 3d region, (d) Valence band spectrum (VBS) for pure Pt, $Pt_{75}Ag_{25}$, $Pt_{50}Ag_{50}$ and $Pt_{25}Ag_{75}$ nanoparticles.

View Article Online
DOI: 10.1039/D2FD00102K

electro-catalytic performance will be explored by the theoretical calculation and physical characterization in our next work. The relationship between deposition time by PLD and electrocatalytic activity toward MOR was also investigated under the same condition as shown in figure-S13. The reaction current of the MOR peak from $Pt_{50}Ag_{50}$ NP prepared for 45 mins is about two times than that of for 25 mins. Besides, the former anchored on the glass carbon electrode is more stabilized than the later after long-term electrochemical measurement. When the deposition time is more than 45 mins, in contrast, the electrocatalytic performance (e. g. deposition for 75 mins) had not improved. This is because electrochemical active area of catalysts decreasing due to excessive grain growth with long-time deposition and it is also a waste of target materials. Hence, 45 mins is considered as the optimal time for this experiment.

Photoelectrochemical performance of PtAg NP catalysts

So far, preparing bimetallic alloy NP with excellent electrocatalytic activity and a strong absorption in visible region, has been a technical challenge. In order to investigate the photoelectrochemical performance of the as-prepared catalyst, the properties of localized surface plasmon resonance (LSPR) was firstly measured by diffuse reflectance UV-vis absorption spectroscopy. Figure S14 depicts the UV-vis diffuse reflectance spectra of as-prepared catalysts including Pt, $Pt_{75}Ag_{25}$, $Pt_{25}Ag_{75}$, and $Pt_{50}Ag_{50}$ NP. As can be seen, PtAg NP exhibit absorption band at wavelength lower than 560 nm which can be ascribed to the SPR effect of Ag in the PtAg NP. With increase of Pt content, the intensity of Ag plasma effect continues to decrease, indicating that Ag play a leading role in the LSPR. The $Pt_{25}Ag_{75}$ and $Pt_{50}Ag_{50}$ NP are found to be red and black colored, respectively, showing a significantly enhanced optical absorption in the visible light region. The absorption spectrum feature of Pt NP indicates that Pt NP do not display LSPR under visible excitation ,which is ascribed to damping mechanism by the d-d bands transitions[61, 62]

The photocurrent response of PtAg NP was investigated under intermittent illumination and solar light using simulated solar light source in 0.1 M N_2-saturated $NaSO_4$ aqueous solution at the potential of 0.745 V vs RHE, as shown in figure 10e. The photocurrent density of $Pt_{50}Ag_{50}$ NP is about 0.015 mA/cm^2 under simulated solar light illumination, which is higher than that of $Pt_{75}Ag_{25}$ NP (about 0.08 mA/cm^2) and is close to that of $Pt_{25}Ag_{75}$ (about 0.015 mA/cm^2). The photo effect of the Pt NP is relatively weak compared to that of PtAg NP, which is in agreement with the LSPR results (see in figure S14).This results indicate that LSPR of PtAg NP irradiated by simulated solar light can significantly enhance the generation of photocurrent in PtAg NP.[63]

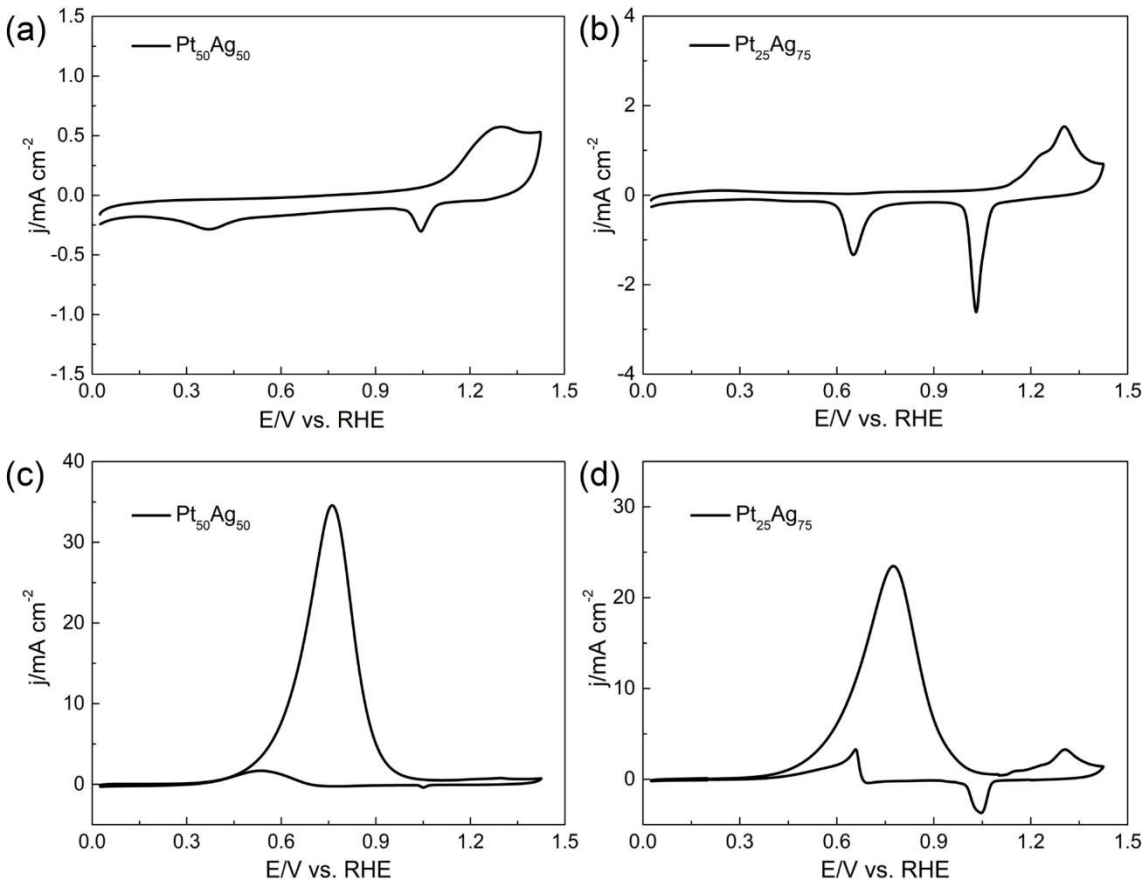

Figure 8. (a, b) Cyclic voltammetry profiles of $Pt_{50}Ag_{50}$ and $Pt_{25}Ag_{75}$ nanoparticles in 1 M KOH solution. (c, d) Cyclic voltammetry profiles during methanol oxidation reaction for $Pt_{50}Ag_{50}$ and $Pt_{25}Ag_{75}$ nanoparticles in 1 M methanol and 1 M KOH solution. All graphs are at a scan rate of 50 mV s^{-1}.

To study the effect of LSPR to the photo-electrochemical property for the PtAg NP, we conducted electrochemical measurements under simulated sunlight illumination as shown in figure 10. For the sake of comparison, the mass activities of three catalysts under sunlight irradiation and dark ambience have been displayed in the figure 10(b, c, d). As showed in figure 10a, the $Pt_{50}Ag_{50}$ NP achieve an enhanced current density of methanol oxidation (4.1 A/mg), under solar light illumination, which is about 16% improvement over $Pt_{50}Ag_{50}$ without light irradiation, indicating that the surface plasmon resonance based on PtAg NP is beneficial for the enhancement of current density. In addition, the onset potential on the PtAg NP modified electrode with solar light illumination is slightly more negative than that without solar light illumination, suggesting that solar light illumination makes the methanol easier to be oxidized on the PtAg NP. $Pt_{50}Ag_{50}$ NP under sunlight irradiation shows the highest mass activity of 4.1 A/mg, which is 5.1 times enhancement than that of commercial Pt/C (0.81 A/mg). The mass activities of $Pt_{25}Ag_{75}$ NP, $Pt_{75}Ag_{25}$ under light irradiation have also displayed improved, reaching potential application including 3.33 A/mg, 1.82 A/mg under light irradiation, which is higher than that of dark ambience (2.91 A/mg, 1.70 A/mg,). Moreover, the effect of natural light on the MOR performance of $Pt_{50}Ag_{50}$NP was also explored. The results reveal that the CV circles for the $Pt_{50}Ag_{50}$NP are not affected by the natural light (figure S15). Figure S16 shows that photocurrent under 468 nm is almost 3 time higher than that of under 640nm illumination, demonstrating that the wavelength range of 400-600 nm has a noteworthy contribution to the generation of photocurrent. These results further demonstrated that both synergistic effects between Ag and Pt, and surface plasmon resonance effect contribute to the enhancement of the electrocatalytic activities towards methanol oxidation.

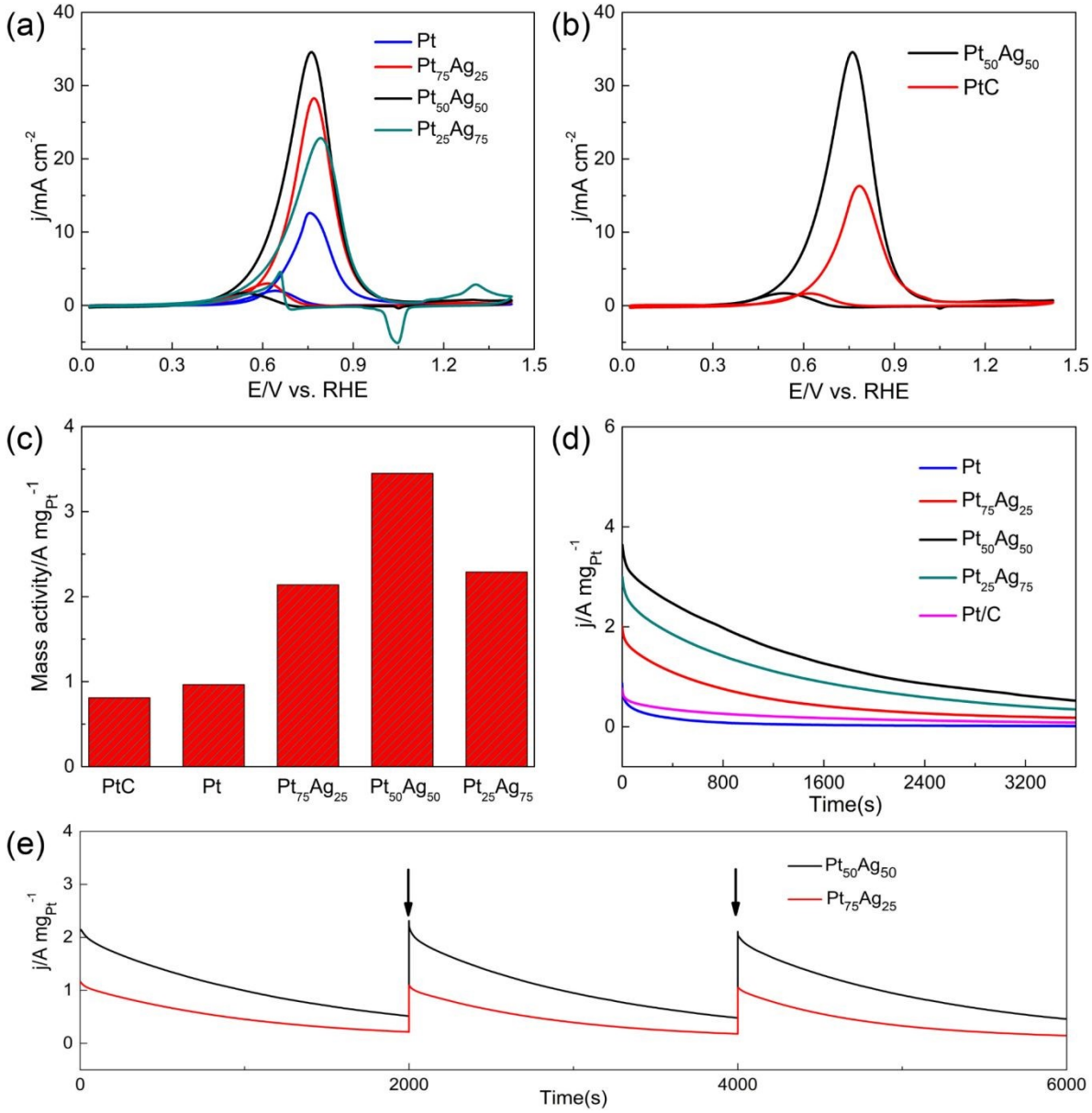

Figure 9. (a) Cyclic voltammetry profiles during methanol oxidation reaction for Pt, $Pt_{75}Ag_{25}$, $Pt_{50}Ag_{50}$ and $Pt_{25}Ag_{75}$ nanoparticles. (b) CV profiles of MOR for $Pt_{50}Ag_{50}$ nanoparticles and the commercial Pt/C catalyst. (c, d) Mass activity and chronoamperometric curves at the potential of 0.745 V vs RHE for the Pt, $Pt_{75}Ag_{25}$, $Pt_{50}Ag_{50}$, $Pt_{25}Ag_{75}$ NP, and Pt/C. Graphs (a, b) are at a scan rate of 50 mV s^{-1}. All graphs above were carried out in 1 M methanol and 1M KOH solution. (e) Long-time durability of $Pt_{50}Ag_{50}$ nanoparticles. These arrows indicate the reactivation of $Pt_{50}Ag_{50}$ and $Pt_{75}Ag_{25}$ catalysts and the replacement of 1 M methanol and 1 M KOH electrolyte.

View Article Online DOI: 10.1039/D2FD00102K

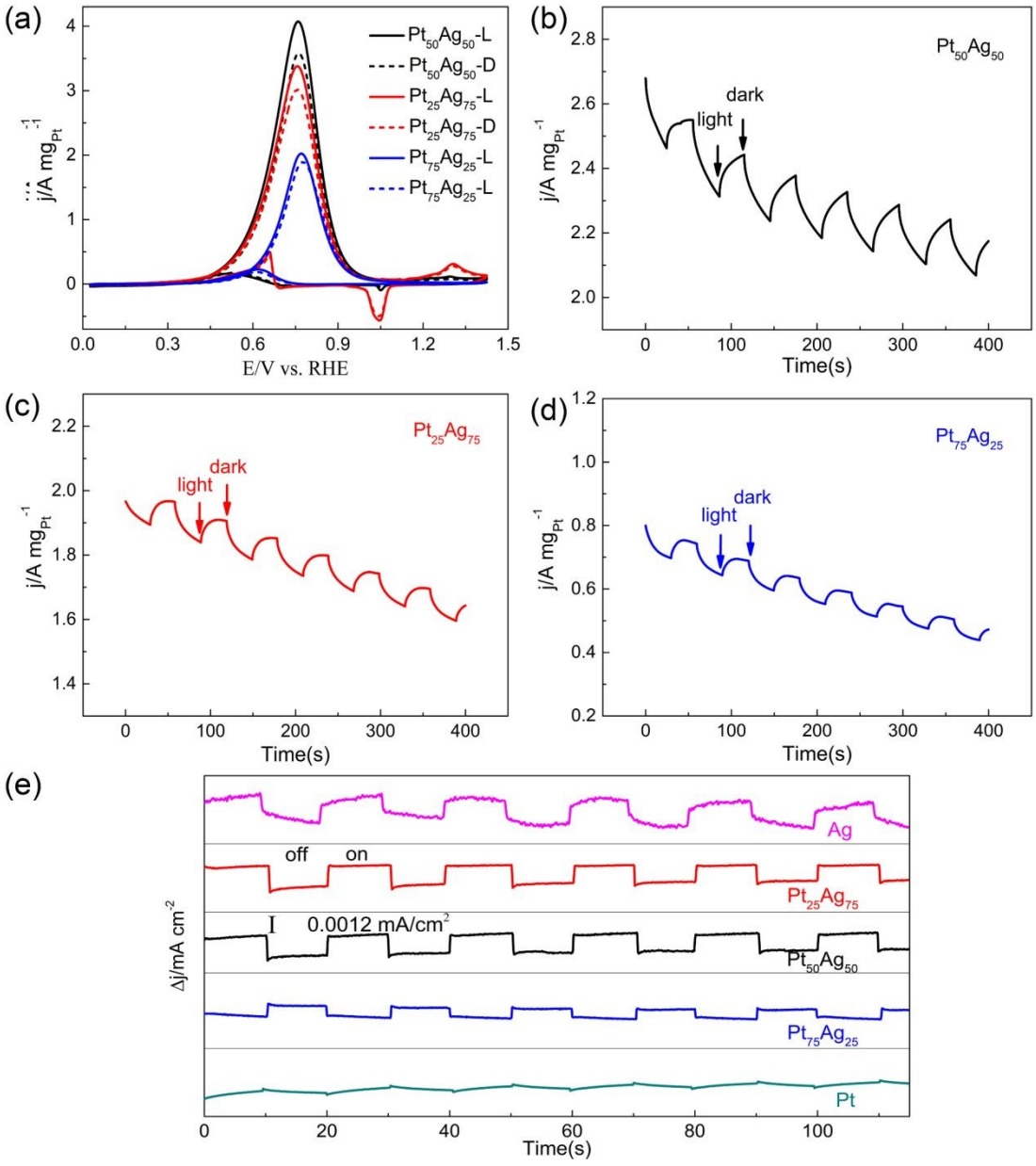

Figure 10. (a) Cyclic voltammetry profiles during methanol oxidation reaction on Pt, $Pt_{75}Ag_{25}$, $Pt_{50}Ag_{50}$ and $Pt_{25}Ag_{75}$ nanoparticles with and without simulated solar light illumination in the 1 M methanol and 1 M KOH solution, (b, c, d) Photocurrent responses of methanol oxidation reaction at the potential of 0.745 V vs RHE for Pt, $Pt_{75}Ag_{25}$, $Pt_{50}Ag_{50}$ and $Pt_{25}Ag_{75}$ nanoparticles, respectively, under simulated solar light which was interrupted every 30s in the 1 M methanol and 1M KOH solution. (e) The photocurrent response of Pt, $Pt_{75}Ag_{25}$, $Pt_{50}Ag_{50}$ and $Pt_{25}Ag_{75}$, Ag NP under intermittent illumination and with solar light by switching simulated solar light source in 0.1 M N_2-saturated $NaSO_4$ aqueous solution at the potential of 0.745 V vs RHE.

Conclusion

In summary, we have demonstrated the syntheses of bimetallic PtAg NP via Pulsed Laser Deposition method and their usage as catalysts for methanol oxidation reduction. The sputtering deposition of PtAg NP was conducted using versatile PtAg targets, which is convenient to modulate PtAg NP composition by varying the number of Ag strips. The as prepared PtAg NP with rough surface and high density of grain boundary present two crystalline phases :1) a majority alloy phase A with a lattice parameter increasing with the proportion of Ag; 2) a second alloy phase B (minority) with a stable lattice parameter close to the pure Pt phase. The obtained structure is not in agreement with homogeneously strained nanoparticles or a perfect crystal. The obtained disordered structures with twin crystal and stacking faults induce small strain, mainly in lattice distortion with respect to the (1 1 1) plane. These structure defects may provide more catalytic active sites for electrochemical catalysis. Especially, $Pt_{50}Ag_{50}$ NP display superior excellent electrocatalytic activities and stabilities towards methanol oxidations in alkaline solution compared to $Pt_{75}Ag_{25}$ NP, $Pt_{25}Ag_{75}$, Pt NP and commercial Pt/C. The superior electrocatalytic performance of $Pt_{50}Ag_{50}$ NP catalyst towards methanol oxidation could be ascribed to unique mesoporous structure as mentioned above, supper refined grains, small strain, and the synergistic effects between Pt and Ag. More interestingly, due to the photoexcitation of the plasmonic $Pt_{50}Ag_{50}$ NP under solar irradiation, a 1.16 times enhancement in catalytic activity for methanol oxidation was observed. The combination of high catalytic activity and surface plasmon resonance effect could pave a new way for developing efficient bimetallic electrocatalysts for alkaline fuel cells in the future.

and their usage
DOI: 10.1039/D2FD00102K

Author Contributions

J. W. and B. P. performed the experimental part, P. A. simulated the XRD of nanoalloy, L. G. and T. J. drew the schematic diagram of dislocation, F. C. designed the research. The authors wrote and commented the paper together.

Conflicts of interest

There are no conflicts to declare.

Acknowledgements

A special acknowledgement goes to Professor Roy L. Johnston, from whose Birmingham Cluster Genetic Algorithm (BCGA), the nanoalloy community benefited greatly. The authors thank Prof. Francesca Baletto and Prof. Alessandro Fortunelli for the invaluable discussion. This work was supported by the National Natural Science Foundation of China (grant no. 51874243, 51271148 and 50971100).

Notes and references

Uncategorized References

1. Q. Tang, F. Chen, Q. Wang, T. Jin, L. Guo, Y. Wu, S. Yu and Z. Li, *Journal of Materials Chemistry A*, 2021, **9**, 23072-23084.
2. X. Zhao, S. Chen, Z. Fang, J. Ding, W. Sang, Y. Wang, J. Zhao, Z. Peng and J. Zeng, *J Am Chem Soc*, 2015, **137**, 2804-2807.
3. M. Ouyang, K. G. Papanikolaou, A. Boubnov, A. S. Hoffman, G. Giannakakis, S. R. Bare, M. Stamatakis, M. Flytzani-Stephanopoulos and E. C. H. Sykes, *Nat Commun*, 2021, **12**, 1549.
4. Q. Wang, F. Chen, Y. Liu, N. Zhang, L. An and R. L. Johnston, *ACS Appl Mater Interfaces*, 2017, **9**, 35701-35711.
5. J. Gu, Y. W. Zhang and F. F. Tao, *Chem Soc Rev*, 2012, **41**, 8050-8065.
6. A. Holewinski, J. C. Idrobo and S. Linic, *Nat Chem*, 2014, **6**, 828-834.
7. M. A. U. Din, F. Saleem, B. Ni, Y. Yong and X. Wang, *ADVANCED MATERIALS*, 2017, **29**, 1604994.
8. Q. Jiang, S. Zhang, J. Jiang, W. Fei and Z. J. A. M. T. Wu, *Advanced Materials Technologies*, 2021, **6**, 2000966.
9. Y. L. Lin, C. Cooper, M. Wang, J. J. Adams, J. Genzer and M. D. Dickey, *SMALL*, 2015, **11**, 6397-6403.
10. M. Shao, Q. Chang, J. P. Dodelet and R. Chenitz, *Chem Rev*, 2016, **116**, 3594-3657.
11. M. Wang, C. Jiang, S. Zhang, X. Song, Y. Tang and H.-M. Cheng, *Nature Chemistry*, 2018, **10**, 667-672.
12. J. Guo, Y. Zhang, L. Shi, Y. Zhu, M. F. Mideksa, K. Hou, W. Zhao, D. Wang, M. Zhao, X. Zhang, J. Lv, J. Zhang, X. Wang and Z. Tang, *J Am Chem Soc*, 2017, **139**, 17964-17972.
13. Z. Zhang, J. Ahn, J. Kim, Z. Wu and D. Qin, *Nanoscale*, 2018, **10**, 8642-8649.
14. Y. Liu, F. Chen, Q. Wang, J. Wang, J. Wang and T. T. Gebremariam, *Journal of Materials Chemistry A*, 2018, **6**, 10515-10524.
15. Y. Yao, Z. Huang, P. Xie, S. D. Lacey, R. J. Jacob, H. Xie, F. Chen, A. Nie, T. Pu, M. Rehwoldt, D. Yu, M. R. Zachariah, C. Wang, R. Shahbazian-Yassar, J. Li and L. Hu, *Science*, 2018, **359**, 1489.
16. P. C. Chen, X. L. Liu, J. L. Hedrick, Z. Xie, S. Z. Wang, Q. Y. Lin, M. C. Hersam, V. P. Dravid and C. A. Mirkin, *SCIENCE*, 2016, **352**, 1565-1569.

17. S. H. Park, H. M. Park, S. S. Han, S. Y. Han and J. Y. Song, *RSC Advances*, 2016, **6**, 3210-3212.
18. K. Kusada, M. Yamauchi, H. Kobayashi, H. Kitagawa and Y. Kubota, *JOURNAL OF THE AMERICAN CHEMICAL SOCIETY*, 2010, **132**, 15896-15898.
19. H. Yan, C. Tian, L. Sun, B. Wang, L. Wang, J. Yin, A. Wu and H. Fu, *Energy Environ. Sci.*, 2014, **7**, 1939-1949.
20. Q. Shi, C. Zhu, C. Bi, H. Xia, M. H. Engelhard, D. Du and Y. Lin, *Journal of Materials Chemistry A*, 2017, **5**, 23952-23959.
21. Z. W. Seh, J. Kibsgaard, C. F. Dickens, I. B. Chorkendorff, J. K. Norskov and T. F. Jaramillo, *SCIENCE*, 2017, **355**, 146-153.
22. Y. Liu, L. Chen, T. Cheng, H. Guo, B. Sun and Y. Wang, *Journal of Power Sources*, 2018, **395**, 66-76.
23. J. Wang, F. Chen, Y. Jin and R. L. Johnston, *Journal of Materials Chemistry A*, 2016, **4**, 17828-17837.
24. J. L. Wang, F. Y. Chen, Y. C. Jin, Y. M. Lei and R. L. Johnston, *ADVANCED FUNCTIONAL MATERIALS*, 2017, **27**, 1700260.
25. S. J. Yoo, S. J. Hwang, J. G. Lee, S. C. Lee, T. H. Lim, Y. E. Sung, A. Wieckowski and S. K. Kim, *ENERGY & ENVIRONMENTAL SCIENCE*, 2012, **5**, 7521-7525.
26. H. Guo, H. Li, K. Jarvis, H. Wan, P. Kunal, S. G. Dunning, Y. Liu, G. Henkelman and S. M. Humphrey, *ACS Catalysis*, 2018, **8**, 11386-11397.
27. H. Kobayashi, H. Morita, M. Yamauchi, R. Ikeda, H. Kitagawa, Y. Kubota, K. Kato, M. Takata, S. Toh and S. Matsumura, *J Am Chem Soc*, 2012, **134**, 12390-12393.
28. K. Kusada, H. Kobayashi, R. Ikeda, Y. Kubota, M. Takata, S. Toh, T. Yamamoto, S. Matsumura, N. Sumi, K. Sato, K. Nagaoka and H. Kitagawa, *JOURNAL OF THE AMERICAN CHEMICAL SOCIETY*, 2014, **136**, 1864-1871.
29. B. Huang, H. Kobayashi, T. Yamamoto, S. Matsumura, Y. Nishida, K. Sato, K. Nagaoka, S. Kawaguchi, Y. Kubota and H. Kitagawa, *J Am Chem Soc*, 2017, **139**, 4643-4646.
30. E. R. Essinger-Hileman, D. DeCicco, J. F. Bondi and R. E. Schaak, *JOURNAL OF MATERIALS CHEMISTRY*, 2011, **21**, 11599-11604.
31. D. H. Lowndes, D. B. Geohegan, A. A. Puretzky, D. P. Norton and C. M. Rouleau, *SCIENCE*, 1996, **273**, 898-903.
32. R. Imbeault, D. Reyter, S. Garbarino, L. Roué and D. Guay, *The Journal of Physical Chemistry C*, 2012, **116**, 5262-5269.
33. E. Irissou, F. Laplante, S. Garbarino, M. Chaker and D. Guay, *JOURNAL OF PHYSICAL CHEMISTRY C*, 2010, **114**, 2192-2199.
34. D. B. Chrisey and G. Hubler, *Pulsed Laser Deposition of Thin Films*, 1994.
35. V. V. Pryadchenko, V. V. Srabionyan, E. B. Mikheykina, L. A. Avakyan, V. Y. Murzin, Y. V. Zubavichus, I. Zizak, V. E. Guterman and L. A. Bugaev, *The Journal of Physical Chemistry C*, 2015, **119**, 3217-3227.
36. S. Chen, S. Thota, X. Wang and J. Zhao, *Journal of Materials Chemistry A*, 2016, **4**, 9038-9043.
37. J. Penuelas, P. Andreazza, C. Andreazza-Vignolle, C. Mottet, M. De Santis and H. C. N. Tolentino, *The European Physical Journal Special Topics*, 2009, **167**, 19-25.
38. P. Andreazza, V. Pierron-Bohnes, F. Tournus, C. Andreazza-Vignolle and V. Dupuis, *Surface Science Reports*, 2015, **70**, 188-258.
39. D. Lahiri, B. Bunker, B. Mishra, Z. Y. Zhang, D. Meisel, C. M. Doudna, M. F. Bertino, F. D. Blum, A. T. Tokuhiro, S. Chattopadhyay, T. Shibata and J. Terry, *JOURNAL OF APPLIED PHYSICS*, 2005, **97**, 094304-094308.
40. P. Durussel and P. Feschotte, *JOURNAL OF ALLOYS AND COMPOUNDS*, 1996, **239**, 226-230.
41. M. H. F. Sluiter, C. Colinet and A. Pasturel, *PHYSICAL REVIEW B*, 2006, **73**, 174204.
42. N. T. Nguyen, J. Nelayah, P. Afanasiev, L. Piccolo, D. Alloyeau and C. Ricolleau, *Crystal Growth & Design*, 2017, **18**, 68-76.
43. J. Pirart, A. Front, D. Rapetti, C. Andreazza-Vignolle, P. Andreazza, C. Mottet and R. Ferrando, *Nat Commun*, 2019, **10**, 1982.
44. A. Caillard, S. Cuynet, T. Lecas, P. Andreazza, M. Mikikian, A. L. Thomann and P. Brault, *Journal of Physics D: Applied Physics*, 2015, **48**, 475302.
45. A. Longo and A. Martorana, *Journal of Applied Crystallography*, 2008, **41**, 446-455.
46. G. Zhang, C. Huang, R. Qin, Z. Shao, D. An, W. Zhang and Y. Wang, *Journal of Materials Chemistry A*, 2015, **3**, 5204-5211.
47. A. Roy, B. Debnath, R. Sahoo, K. R. S. Chandrakumar, C. Ray, J. Jana and T. Pal, *JOURNAL OF PHYSICAL CHEMISTRY C*, 2016, **120**, 5457-5467.
48. S. Wang, F. Yang, S. P. Jiang, S. Chen and X. Wang, *Electrochemistry Communications*, 2010, **12**, 1646-1649.
49. C. Koenigsmann and S. S. Wong, *Energy Environ. Sci.*, 2011, **4**, 1161-1176.
50. G. Zhang, Z. Yang, W. Zhang and Y. Wang, *Journal of Materials Chemistry A*, 2016, **4**, 3316-3323.
51. X. Yuan, X. Jiang, M. Cao, L. Chen, K. Nie, Y. Zhang, Y. Xu, X. Sun, Y. Li and Q. Zhang, *Nano Research*, 2019, **12**, 429-436.
52. D. A. Slanac, W. G. Hardin, K. P. Johnston and K. J. Stevenson, *J Am Chem Soc*, 2012, **134**, 9812-9819.
53. J. S. Guo, A. Hsu, D. Chu and R. R. Chen, *JOURNAL OF PHYSICAL CHEMISTRY C*, 2010, **114**, 4324-4330.
54. T. Huang, S. Mao, G. Zhou, Z. Zhang, Z. Wen, X. Huang, S. Ci and J. Chen, *Nanoscale*, 2015, **7**, 1301-1307.
55. F. F. Ren, C. Q. Wang, C. Y. Zhai, F. X. Jiang, R. R. Yue, Y. K. Du, P. Yang and J. K. Xu, *JOURNAL OF MATERIALS CHEMISTRY A*, 2013, **1**, 7255-7261.
56. M. Niu, W. Xu, S. Zhu, Y. Liang, Z. Cui, X. Yang and A. Inoue, *Journal of Power Sources*, 2017, **362**, 10-19.
57. P. Gnanaprakasam, S. E. Jeena and T. Selvaraju, *Journal of Materials Chemistry A*, 2015, **3**, 18010-18018.
58. H. Li, C. Tsai, A. L. Koh, L. Cai, A. W. Contryman, A. H. Fragapane, J. Zhao, H. S. Han, H. C. Manoharan, F. Abild-Pedersen, J. K. Norskov and X. Zheng, *Nat Mater*, 2016, **15**, 364.
59. H. Wang, S. Xu, C. Tsai, Y. Li, C. Liu, J. Zhao, Y. Liu, H. Yuan, F. Abild-Pedersen and F. B. J. S. Prinz, 2016, **354**, 1031-1036.
60. M. Ayán-Varela, R. Ruiz-Rosas, S. Villar-Rodil, J. I. Paredes, D. Cazorla-Amorós, E. Morallón, A. Martínez-Alonso and J. M. D. Tascón, *Electrochimica Acta*, 2017, **231**, 386-395.
61. A. Wood, M. Giersig and P. Mulvaney, *The Journal of Physical Chemistry B*, 2001, **105**, 8810-8815.
62. P. Mulvaney, *Langmuir*, 1996, **12**, 788-800.
63. S. C. Lin, C. S. Hsu, S. Y. Chiu, T. Y. Liao and H. M. Chen, *J Am Chem Soc*, 2017, **139**, 2224-2233.